applied sciences

MDPI

Article

Characterization of Defects by Non-Destructive Impulse Excitation Technique for 3D Printing FDM Polyamide Materials in Bending Mode

Fatima-Ezzahrae Jabri [1,2], Imi Ochana [1,3], François Ducobu [3], Rachid El Alaiji [2] and Anthonin Demarbaix [1,*]

[1] Science and Technology Research Unit, Haute Ecole Provinciale de Hainaut Condorcet, Boulevard Solvay 31, 6000 Charleroi, Belgium; fatimaezzahrae.jabri1@etu.uae.ac.ma (F.-E.J.); imi.ochana@condorcet.be (I.O.)
[2] Laboratory of Innovative Technologies (LTI), National School of Applied Sciences, Road Ziaten Km 10, Tangier Principale, Tangier 90060, Morocco; relalaiji@uae.ac.ma
[3] Machine Design and Production Engineering Laboratory, Research Institute for Science and Material Engineering, University of Mons, 7000 Mons, Belgium; francois.ducobu@umons.ac.be
* Correspondence: anthonin.demarbaix@condorcet.be

Abstract

The presented article analyzes the impact of internal defects on the modal responses of polyamide parts subjected to bending. Samples with defects of various sizes (0, 3, 5, 7, and 10 mm) located at the neutral bending line were tested. Modal properties were measured via an acoustic and a vibration sensor, using impulse excitation and fast Fourier transform (FFT) analysis. Modal properties include peak frequency, damping and amplitude. Non-defective samples show lower peak frequency and stronger amplitude for both detectors. Moreover, defects larger than 3 mm have minimal impact on peak frequency. The vibration detector is more sensitive to delamination presented at 7 and 10 mm defects. In addition, elevated peak frequency at 3 mm is the result of local hardening at the defect edge. Moreover, a neutral line position reduces damping when the defect size approaches 5 mm. Conversely, acoustic detectors ignore delamination and reveal lower damping and amplitude at 7 and 10 mm defects. Furthermore, internal sound diffusion from 3 and 5 mm defects enhances air losses and damping. Acoustic detectors only evaluate fault size and position, whereas vibrational detectors may detect local reinforcement and delamination more easily. These results highlight the importance of choosing the right detector according to the location, size, and specific modal characteristics of defects.

Keywords: fused deposition modeling; polyamide; internal defect; impulse excitation technique and Fast Fourier Transform (FFT)

Academic Editor: Xiaodong Shi and Michel Darmon

Received: 18 June 2025
Revised: 16 July 2025
Accepted: 22 July 2025
Published: 25 July 2025

Citation: Jabri, F.-E.; Ochana, I.; Ducobu, F.; El Alaiji, R.; Demarbaix, A. Characterization of Defects by Non-Destructive Impulse Excitation Technique for 3D Printing FDM Polyamide Materials in Bending Mode. *Appl. Sci.* **2025**, *15*, 8266. https://doi.org/10.3390/app15158266

1. Introduction

Fused Deposition Modeling (FDM) creates 3D-printed objects by extruding melted filaments in layers using a nozzle. Typical materials include polyamide, polycarbonate (PC), polylactic acid (PLA), and polyether ether ketone (PEEK) [1,2]. Such materials are well-suited for structural, automotive, and aerospace applications [3], due to their customized mechanical properties and high strength-to-weight ratios [4]. Nevertheless, defects like porosity, delamination, and fiber misalignment can be introduced during the layer-by-layer deposition process, which can affect the structural integrity of the material [5]. Other factors like material properties, printing parameters, and cooling dynamics [6] can interact in complicated ways, which can lead to other flaws such

as warping, stringing, and under-extrusion [7]. Moreover, Baechle-Clayton et al. [7] found that software, build strategy, and hardware limitations can all lead to process-associated issues. Consequently, the use of non-destructive testing (NDT) methods is vital in the identification and characterization of defects in 3D-printed parts. A number of NDT methods have been used to evaluate additively built parts for imperfections such as thermography [8], X-ray computed tomography [9], eddy current testing [10], and ultrasonic testing [11]. The impulse excitation technique (IET), also known as tap testing, is one of the most simple and efficient ways to find imperfections in composite structures [12]. This technique has undergone updates for various uses, such as identifying insulation flaws, evaluating composite damage [13], and determining dynamic moduli at high temperatures [14]. IET's simplicity, low cost, and great precision make it useful for non-destructive testing [15]. In addition, scientists have created automated technologies to make impact testing more accurate and repeatable [16,17]. The technique also depends on identifying the vibration and acoustic response that a tapped structure generates [13]. In order to detect defects like holes, fissures, and material irregularities, these methods examine the vibrational properties of objects [18]. In this context, vibro-acoustic techniques have demonstrated a high sensitivity for detecting gaps in safety components, agro-products, and composite structures [12]. They entail subjecting a structure to an impact force and then examining the vibrations or acoustic emissions that result [15,19]. Therefore, the efficiency of the approach is dependent on the examination of dynamic factors such as the response frequency and damping ratio [14]. Here, the fast Fourier transform (FFT) establishes a relationship between amplitude and frequency by mapping the amplitude of each frequency component to its corresponding frequency. This allows the FFT to provide a frequency domain representation of a signal. Moreover, the technique is flexible enough to accommodate multi-modal analysis, which includes torsional and flexural excitations [20]. Several applications focus on building dispersion curves and material characteristics [21]. In terms of this, FFT analysis of flexural free vibration is also utilized to calculate the viscoelastic characteristics of fiber-reinforced composites [22]. In this context, dynamic mechanical thermal analysis and longitudinal free vibration testing have shown consistency in assessing the viscoelastic characteristics of polymer composites [23]. FFT can also characterize damage in carbon fiber/epoxy composites through acoustic emission analysis [17]. However, FFT has limitations in analyzing non-stationary signals. In addition, Brown et al. [24] emphasize in their work that combining accelerometer and microphone data can enhance our understanding of the underlying physical principles [25]. Furthermore, Raza et al. [26] utilized Macro Fiber Composite (MFC) actuators for active vibration control in 3D-printed structures made from polylactic acid (PLA) and its composites, employing a laser vibrometer to analyze natural frequencies and bending modes. They innovatively identified the optimal phase and amplitude of the input voltage for the MFC actuators through an incremental domain search. Likewise, Benabderazaz et al. [27] explored the application of advanced techniques of 3D-printed biocomposite created from Lygeum spartum fibers and PLA such as digital image correlation and acoustic emission to evaluate mechanical performance during flexural testing. Moreover, Bhudolia et al. [28] presented a new method for creating thermoplastic tubular composites reinforced with carbon fiber, utilizing the Bladder-Assisted Resin Transfer Molding (B-RTM) process. The new impact flexural test showed that these composites outperformed traditional carbon/epoxy tubes, achieving 16.3% higher peak load and 18.9% more major damage energy. Moreover, Vigneshwaran et al. [29] investigated the acoustic properties of FDM-printed PLA wood composites by examining tensile and flexural strengths based

on varying parameters, ultimately finding the optimal conditions for strength. The new acoustic feature developed involved printing micro-perforated panels with different perforation sizes and shapes to analyze their sound transmission loss and absorption characteristics. An acoustic vibration test method has been used by [30] to assess the acoustic performance of fiber-reinforced composites made from hemp and ramie in epoxy. This approach systematically evaluates how factors like impulse, humidity, and thickness influence the composites' acoustic response. Also, Heinrich et al. [31] introduced a method for detecting structural defects in machine-made parts using acoustic resonance testing and synthetic training data generated through simulations. The novel aspect is the shift from traditional experimental training data to simulated data, enhancing the classification of defective and non-defective components. In the reference [32], the authors examine the acoustic emission method to track the loading and failure mechanisms of carbon/epoxy composites. The new aspect of this study is the assessment of the frequency range of flexural loading concerning the bending behavior of the composite and its acoustic signals. IET is emerging as a powerful non-destructive testing method for additively manufactured (AM) parts. IET also can classify parts manufactured with different process parameters [30] and detect microstructural defect [24]. In this context, there is a lack of explicit focus on defect characterization for polyamide parts and identification of their impact on vibrational and acoustic sensor responses. Therefore, we need to explore where the variation in defect size enhances or diminishes damping, amplitude, and frequency responses. This study focuses on the application of impulse excitation techniques to evaluate defects in FDM-printed polyamide in flexural mode. To achieve this, we created defects inside the piece to analyze their impact on its frequency response and damping using acoustic and vibrational detectors. The vibration detected by the vibration detector is the result of the displacement probe, which precisely measures the microscopic displacement at the needle's point. Meanwhile, acoustic detectors or microphones employ cells to pick up environmental sound waves and record the resulting frequency. Consequently, both detectors analyze the recorded signal to derive resonance frequencies. So, this study intends to experimentally examine the modal responses of FDM-printed polyamide carbon fiber composite components utilizing acoustic and vibration sensors. Specifically, our study intends to investigate how modal responses, such as peak frequency, amplitude, and damping, are affected by the size of internal defects situated along the neutral line axis. Hence, the paper is structured as follows: first, we present the materials, experimental plan, and impulse excitation technique principles used to detect internal defects. Secondly, the experimental results and their implications for frequency and damping assessment for different defect sizes are analyzed. Section 3 summarizes the key findings.

2. Materials and Methods

This section describes the materials used, the equipment needed for the experiments, and the test procedure.

2.1. Materials

Polyamide 12 filament reinforced with 10% of carbon fiber, namely, Smooth PA (Anisoprint, Singapore, Singapore) was used to evaluate 3D-printed FDM parts. PA smooth was in filament form with a diameter of 1.75 mm and was made by Polymaker and Anisoprint group. It provided improved surface quality, strength, and warping. Compared to other polyamide filaments on the market, Smooth PA features low-moisture-absorption

and anti-warping technology. The main properties and recommended margins based on Polymaker's datasheet for the printing of used filament are presented in Table 1.

Table 1. Properties of printing filament.

Filament	PA Smooth
Color	Matt black
Diameter (mm)	1.75
Print temperature (°C)	260–270
Print speed (mm/s)	20–50
Bed temperature (°C)	45–60
Fiber type	Carbon
Fiber content (%)	10
Density (g/cm^3)	1.06 with ISO 1183 standards [33]

2.2. FDM Printer and Sample Preparation

An Anisoprint Composer A4 printer was used to manufacture all the test specimens in this work. This FDM printer uses various thermoplastics materials including PETG, PLA, PC, and PEEK. The build volume has dimensions of 297 mm × 210 mm × 140 mm, with a minimum layer thickness of 0.06 mm and a nozzle diameter of 0.4 mm. Table 2 presents the characteristics of the Anisoprint and the printing parameters used in this study. The model used in this study is based on the ceramic reference beam dimensions in accordance with the ASTM 1876-01 standard [34] (100 mm × 24 mm × 10 mm). We printed samples that contained internal defects in the middle of the sample with a square shape that varied between no defect, 3, 5, 7, and 10 mm (Table 3 and Figure 1) with the same height of 0.25 mm. In order to simulate the appearance of delamination or porosity associated with actual parts, these defects are created by intentionally not depositing material at specific locations on the print head. To evaluate the influence of modest geometrical modifications on the structure without significantly perturbing the global characteristics of the 3D-printed component, the holes are made in the center of the samples' thickness, at the neutral line of bending mode. Generally, the samples were printed with ±45° of print orientation and a print speed of 40 mm/s. In each FDM experiment, three samples for each group of defect size were consistently produced under identical conditions to ensure reliable data. CAD designs were drawn and visualized in CATIA V5 software and transferred to 3D-printable format using AURA software for G-code generation.

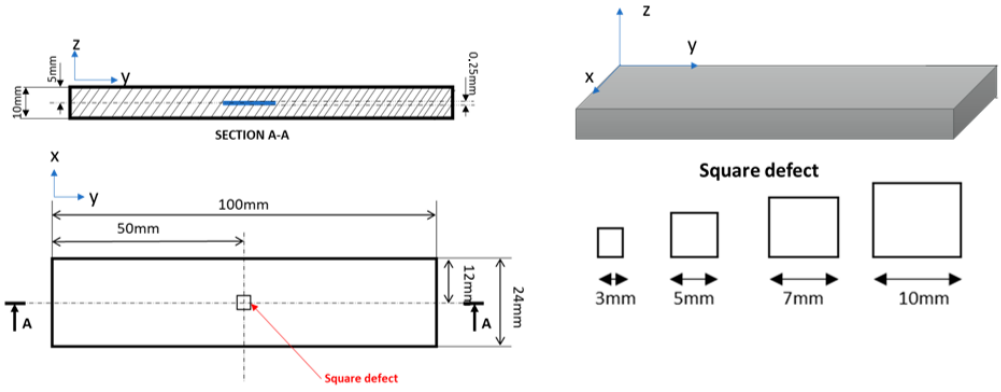

Figure 1. Internal defect position and dimensions of 3D polyamide parts.

Table 2. Anisoprint machine specification and process parameters.

3D Printer	Anisoprint
Print volume	297 mm × 210 mm × 140 mm
Control software	Aura version 2.5.8
Minimum layer thickness	0.06 mm
Nozzle diameter	0.4 mm
Building plate temperature (°C)	60
Nozzle temperature (°C)	265
Print speed (mm/s)	40
Printing orientation	±45°
Layer thickness	First layer: 0.25 mm Other layers: 0.1 mm

Table 3. Test case overview.

Test Case	No Defect/With Defect	Defect Dimensions
1	No defect	_____
2	With defect	3 mm
3	With defect	7 mm
4	With defect	5 mm
5	With defect	10 mm

2.3. Impulse Excitation Test

In this study, a GrindoSonic system (KU Leuven, Leuven, Belgium) enabled the non-destructive evaluation of both acoustic and vibration responses from samples subjected to impact testing. In order to identify the effect of defect size variation, the GrindoSonic MK7 device measured resonance frequencies and damping. The specimen's dynamic behavior during hammer excitation was observed in our investigation through a bending test. The configuration, including the placement of the hammer and the detectors, is depicted in Figures 2–4, which illustrate the method of analysis and sensor placement during the experiment. First, using two nodal supports, the beam was positioned on nodes 22.4% from either side of the part. In order to create vibrations, the setup consisted of tapping the samples with a steel hammer that had a 10 mm shaft ball diameter. Two detectors were used: one for acoustic signals and another for vibration signals. The steel hammer was applied at the center of the beam to ensure consistent excitation, while the vibration detector was placed at the intersection of the centered horizontal line and the nodal line to capture the vibrational response in the flexural mode. Its sensitivity to displacement in the direction of the black point detector makes it possible to identify a particular minimum vibrational amplitude at the nodal support shown in Figure 4. Simultaneously, the acoustic detector was positioned at the center end line of the beam no matter which side was chosen to record the generated sound waves and maximum vibration amplitude. This dual detection method enabled the analysis of both the acoustic and vibrational characteristics of the material. Six independent hammer taps were performed for each sample, and the FFT was obtained from the machine. Further, Table 4 describes the characteristics of the GrindoSonic machine, including its specifications and capabilities. After collecting data using both the acoustic and vibrational detectors, the frequency and damping responses of the samples were determined by data analysis.

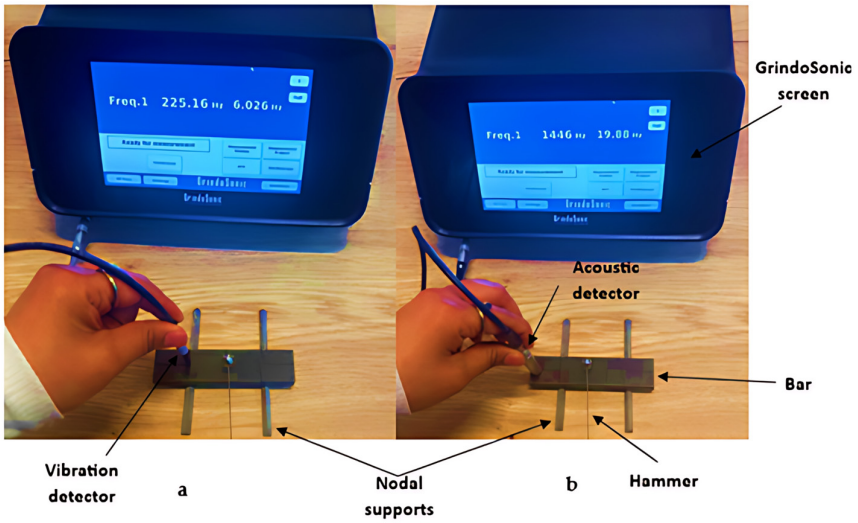

Figure 2. Experimental setup for impulse excitation technique in flexion mode with (**a**) vibration detector, (**b**) acoustic detector.

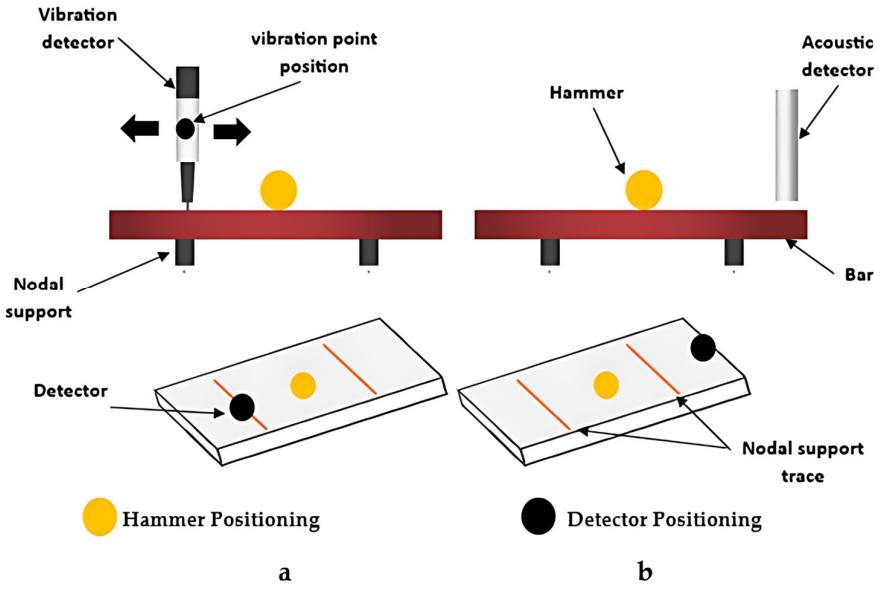

Figure 3. (**a**) Vibration bending test, (**b**) acoustic bending test for PA Smooth.

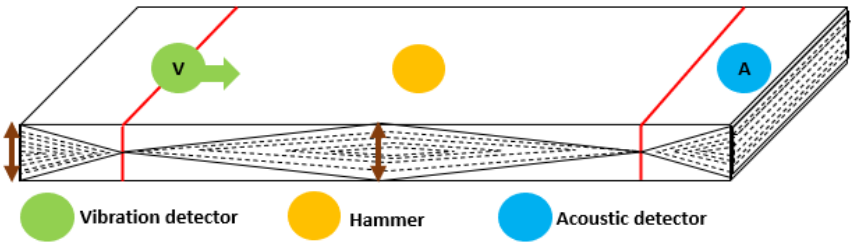

Figure 4. Flexural vibrational mode: activation and monitoring.

The results of an impulse-tested fast Fourier transform (FFT) curve are presented in Figure 5. Using a vibration detector, this figure shows the experimental results for the frequency response of the bending mode of a ceramic reference beam. The ceramic reference bar is completely dry, free of defects, and in its original condition. Accordingly, the black curve represents the excitation's frequency response as computed using standard FFT approaches. Further, a fitted line is displayed through the plotted points on the red curve.

In this regard, the GrindoSonic system applies a Lorentzian function fitting using non-linear least-squares techniques. The variables ζ and Δf, representing damping and half-height width, respectively, were determined using this approach. In addition, a damping value was placed near the peak with the highest amplitude. Here, the 3 dB bandwidth approach was used to compute damping, determined by fitting the resonance peak to a function that determined the peak's width at half its height. Therefore, the following Equation (1) describes the unitless physical value of the damping ratio:

$$\zeta = \frac{\Delta f}{2 f_0} \tag{1}$$

where ζ defines the fraction of critical damping or damping ratio, Δf is the 3 dB bandwidth in Hz, and f_0 denotes the undamped natural frequency in Hz. Hence, the material's natural resonance can be found by locating its peak frequency; examining these results can help us better understand how defect size affects resonance behavior.

Table 4. GrindoSonic MK7 machine specifications.

Properties	Specification
Frequency range	20 Hz–150 kHz
System accuracy	Absolute accuracy greater than 0.005%
Measurement resolution	1/10,000,000 (0.1 ppm)
System repeatability	3/10,000,000 (0.3 ppm)
Sampling frequency	10 kHz–1 MHz
Number of samples	1024–524,288
Power supply	100–240 VAC/50–60 Hz/42W
Protection classification	IP50

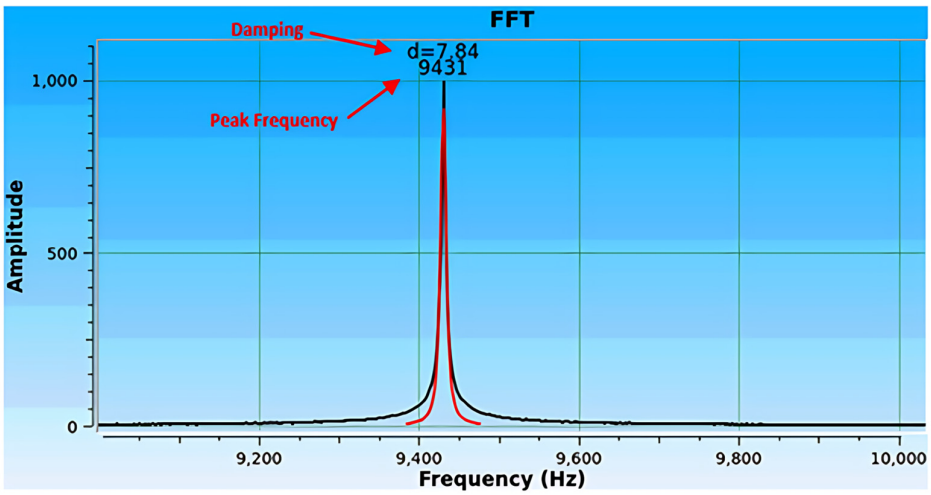

Figure 5. FFT analysis curve.

2.4. X-Ray Inspection

An initial phase in the process involved using the RT method on the X-RIS Dxbox-200 X-ray Inspection Cabinet from WAN in Charleroi, Belgium, to confirm the existence and position of any pre-existing faults in the part that was specifically developed. The capacity to identify internal defects in 3D-printed parts can be evaluated with the help of this study, which serves as a control and identification of any potential variables that could affect the outcomes. Hence, radiographs of the front and side of the component were captured.

3. Results and Discussion

The Results Section comprises five sections. The first describes the visual assessment of printed samples with the naked eye. The second presents data from X-ray radiography, used to detect the internal defects created in the analyzed parts. The third one emphasizes the mass measurement of each defective printed part. The fourth covers the results obtained by the acoustic detector, in the form of frequency peaks, amplitude, and damping. The fifth sub-section presents the vibration measured by the vibration detector, also including the frequency peaks, damping, and amplitude values associated with each defect.

- Visual inspection

All parts were examined with the naked eye before being tested. No major visible defects were observed. In addition, the presence of lines on the sides of samples indicates the interfaces between each printed layer, identified as traces of printed layers, as shown in Figure 6. However, defect-free parts show no traces for any printed layer.

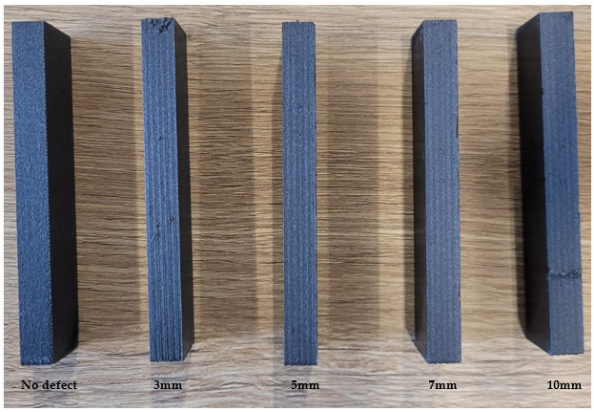

Figure 6. Side view of printed samples showing layer deposition traces.

- X-ray inspection

Figure 7 displays the radiographic image of the beams, with and without defects, illustrating the defects that have been detected. Simply visible are all defects ranging in square dimensions from 3 to 10 mm, with a depth of 0.25 mm. The dimensions and the square structure of the defects can be precisely ascertained. Nevertheless, a single hole is seen in parts that are free of defects, whereas two holes are found in parts that have 7 mm defects. In addition, a delamination is visible in the side view of the 7 and 10 mm defective components. Nonetheless, due to the 45° printing angle of the parts, a defect printing line indicates the direction of printing. The systematic defect is likely caused by the 45° print direction, where the head always starts near the edge, creating a visible direction mark at the same spot with each layer.

- Mass Characterization

The masses obtained for each defect size are listed in Table 5. A highly accurate VWR model M254Ai-M electronic balance (BEL Engineering SRL, Monza, Italy), capable of holding up to 250 g of material, was used to measure the mass of each sample (see Figure 8). Its accuracy is 0.0001 g. With standard deviations less than 0.5, the measured masses show consistent values for many measurements. A slight variation in mass is observed when comparing defective and non-defective samples. Among the parts tested, the sample with the 3 mm internal defect has the highest mass (23.648 g), while the parts without internal defects have the lowest mass (23.408 g). As shown in Figure 9, a slight increase in mass is due to local hardening at the edges of the defects during printing.

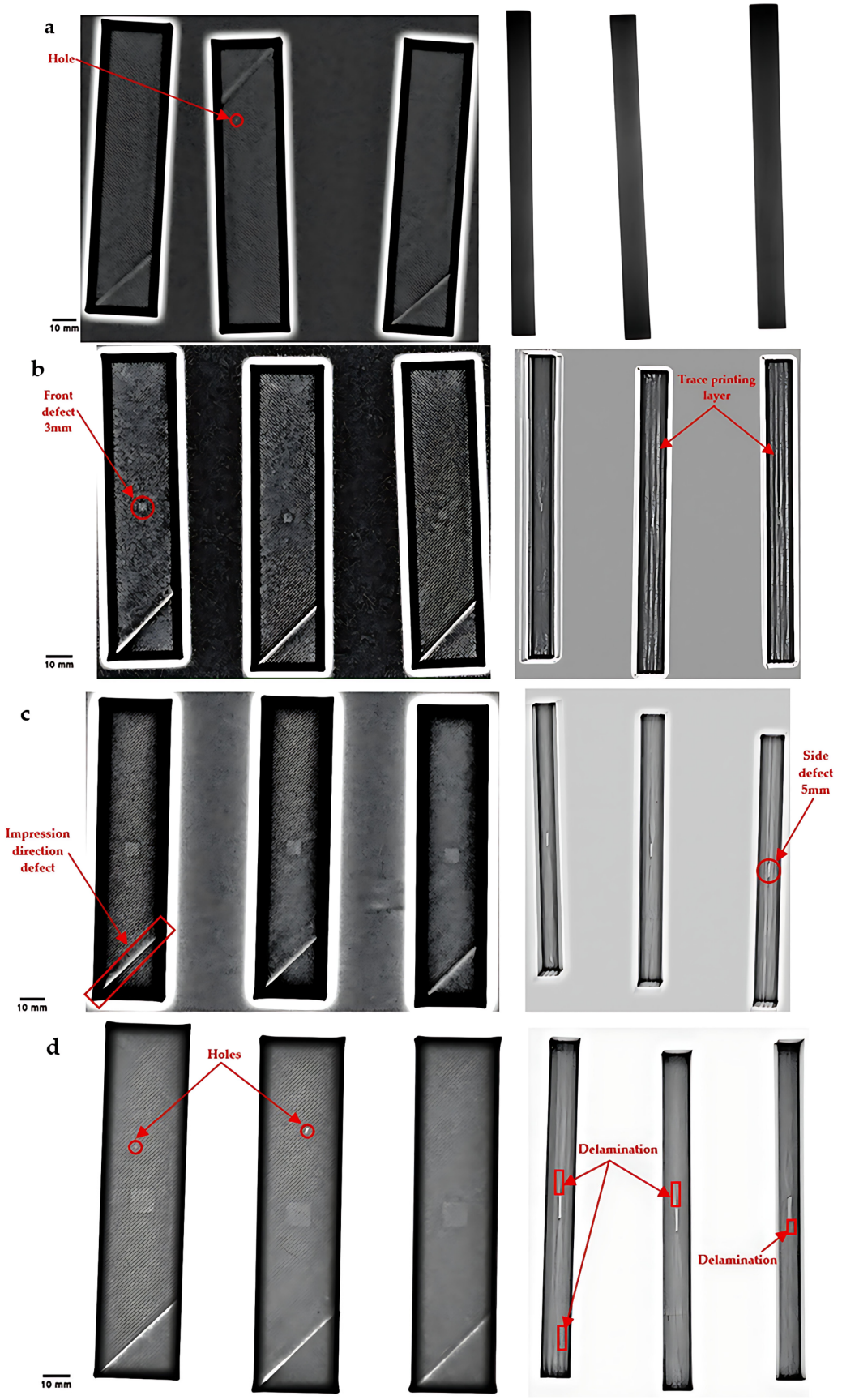

Figure 7. *Cont.*

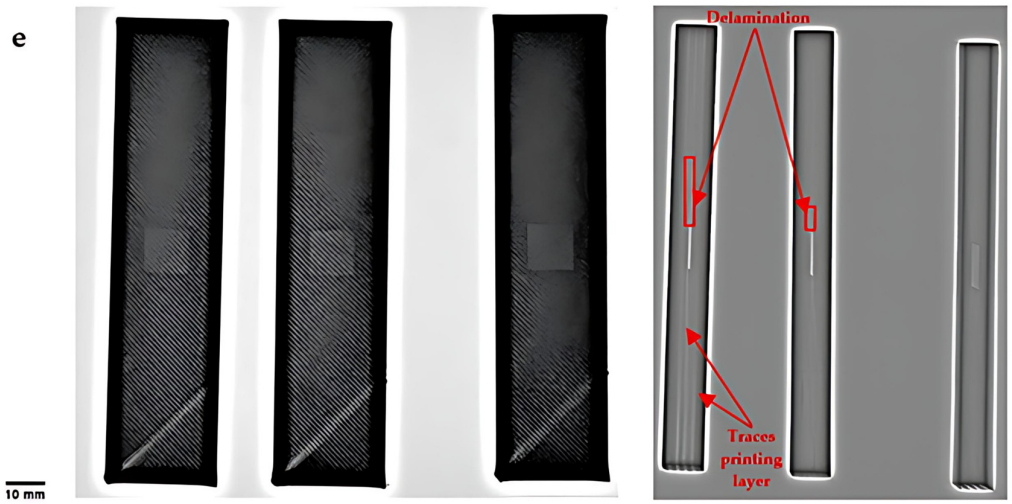

Figure 7. X-ray scans of beams: front and side views of samples with (**a**) no defects and (**b**) 3 mm, (**c**) 5 mm, (**d**) 7 mm, and (**e**) 10 mm defects.

Table 5. Measured masses for each defect size.

Defect Size	Defect-Free		3 mm		5 mm		7 mm		10 mm	
	Average	Standard Deviation	Average	Standard Deviation	Average	Standard Deviation	Average	Standard Deviation	Average	Standard Deviation
Mass (g)	23.408	0.028	23.648	0.056	23.585	0.457	23.647	0.057	23.644	0.049

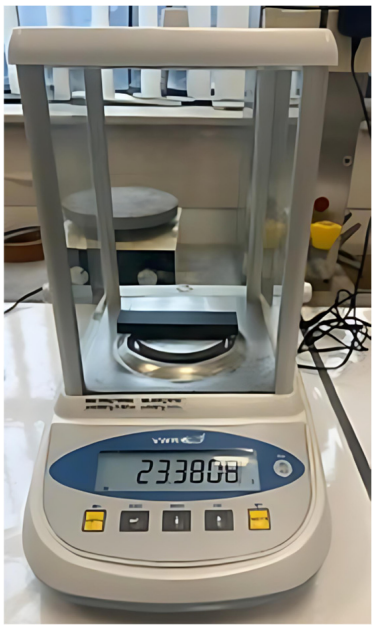

Figure 8. Sample mass measurement.

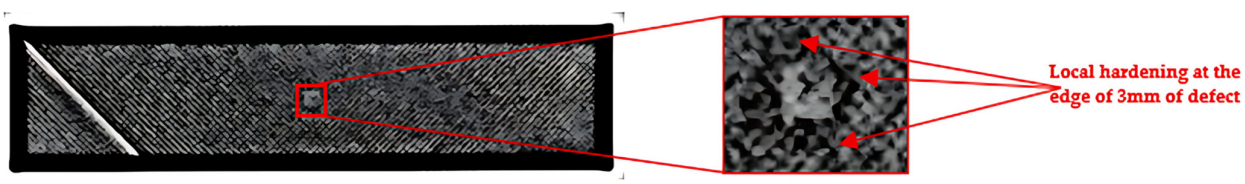

Figure 9. Local hardening in defective 3 mm samples (X-ray image).

- Acoustic detector

Table 6 shows the mean values for maximum frequency and damping extracted from the FFT curves. The mean values represent the average of six taps of three samples from each fault situation. As can be seen, the maximum frequency is minimal in cases where there is no defect. However, a higher frequency peak is recorded at 10 mm of defect, proving that the frequency is sensitive to the presence of defects in the neutral line and especially at 10 mm of defect. Low damping is also observed at 10 mm of defect, which explains why damping reacts differently from peak frequency to defect variation.

Table 6. Defect size-dependent averages for frequency peak and damping using acoustic detector.

Test Type	Acoustic Test									
Defect Size	Defect-Free		3 mm		5 mm		7 mm		10 mm	
	Average	Standard Deviation	Average	Standard Deviation	Average	Standard Deviation	Average	Standard Deviation	Average	Standard Deviation
Frequency peak (Hz)	1390.055	5.185	1426.138	7.090	1420.044	6.833	1431.233	7.225	1433.005	7.803
Damping	22.292	0.886	22.716	0.769	25.981	1.806	21.622	0.529	21.350	0.495

Figure 10 reveals the average peak frequency of samples as a function of the defect size. The results indicate a notable increase in peak frequency from 1390.055 to 1426.139 Hz when comparing samples without defects to those with a defect dimension of 3 mm squared. This suggests that the acoustic detector effectively detects the presence of defects that are introduced due to better air and structure coupling. In this defect position, local stiffness increases at the hardened edge of the 3 mm defective sample, as shown in Figure 9. This reduces inertia and accelerates response to vibratory forces. From 3 mm to 5 mm of defect, a slight decrease in peak frequency is observed, dropping to 1420.0444 Hz. This is consistent with the fact that the 3 mm samples indicate local hardening, which causes the peak frequency to be higher than it would be with a 5 mm defect, thus breaking the linear relationship between the frequency peak and the defect size. However, from 5 to 10 mm, a slight rise is recorded. This is due to the increase in defect size, particularly in 7 and 10 mm beams that may slightly modify the vibration patterns. In addition, the error bars indicate the dispersion of measurements for each test case. In this respect, these bars overlap between 3 and 10 mm defects, meaning that differences in defect size are not noticeable in this test range. This may be due to the three spatial positions of the defect on the neutral bending axis. As the defect is located on the neutral flexural axis, it interacts less with the propagating wavefronts and has a smaller influence on the modal excitation. Consequently, varying the defect size beyond 3 mm has less of an effect on the peak frequency.

The implication of the introduced defect size on the damping response is displayed in Figure 11. A progressive increase in damping is observed as the square void grows from a no-defect state to 5 mm. This elucidates that small 3 and 5 mm defects can create internal sound diffusion and vibratory disorder. Hence, this increases air losses and apparent damping. Conversely damping decreases from 5 mm to 10 mm. This suggests that high defect size (7 and 10 mm) interrupts external wave transmission, and therefore, less energy goes into the air. As the acoustic detector picks up waves radiated by the surface, the acoustic sensor shows low sensitivity to the delamination present in beams of 7 and 10 mm (Figure 7d,e), because the defect size is small compared to the acoustic wavelength, leading to weak scattering. This confirms that damping with an acoustic sensor does not reflect the structural integrity of the 3D-printed part.

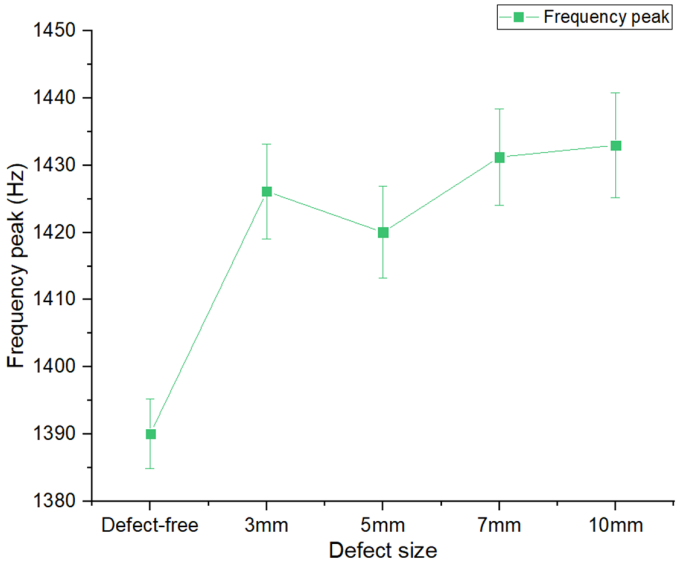

Figure 10. Variation in frequency peak with defect square size.

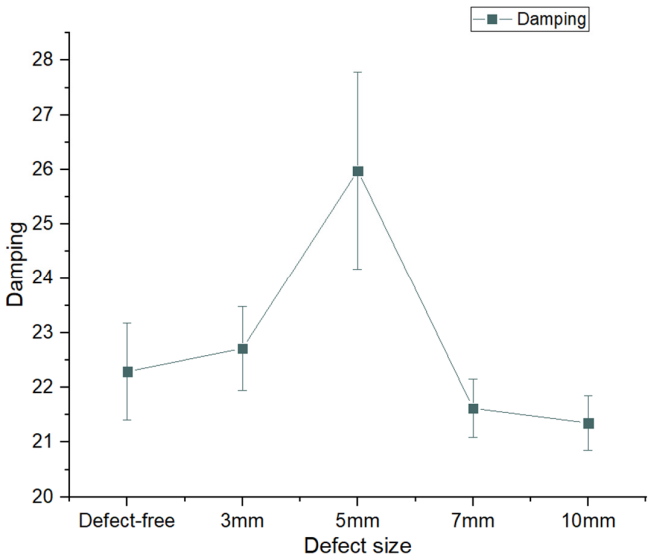

Figure 11. Effect of damping on defect square size.

Based on six taps of three samples for each defect size, Figure 12 displays the average Fourier transform (FFT) curves obtained with MATLAB R2022b software. A fast Fourier transform (FFT) was performed on the vibration signal of the average of 18 taps of all the three samples. To conduct the analysis, a script in MATLAB R2022b was used to visualize the FFT spectra and apply a Lorentzian-type curve fitting. Two distinct peaks can be noticed in Figure 12. The first, identified in red, is the natural frequency, which is a measure of the system's intrinsic resonance. The most elevated frequency between 0 and 1000 Hz is the second peak, named Peak 2, revealing a recurrent vibrational mode in all samples marked with sky blue. In comparison to samples with defects of different sizes, those with no defects in the 0 to 1000 Hz range exhibit a notably higher number of harmonics. These samples therefore offer better wave propagation, and the absence of defects does not disrupt the continuity of the material. For all defect sizes, Peak 2 is shown in Figure 10 at a consistent frequency of 73.27 Hz. This second frequency peak is not affected by changes in defect size. This may be explained by the fact that our defect is placed on the neutral line, which has no major impact on frequency. This suggests that Peak 2 may be related to the location of the defect, which had no real impact on Peak 2's frequency. In contrast, defect

detection is more pronounced at the amplitude of the second peak. At this point, the data obtained remain consistent with bending behavior. Nevertheless, amplitude variations allow us to formulate a complementary hypothesis concerning the possible intervention of an additional stress mode such as torsion or a combination of the two. As the defect size rises, nonetheless, the amplitude of Peak 2 typically decreases. Another explanation is that larger defects (7 and 10 mm) exhibit delamination around the edges of the defect, which generates internal friction, creating a local loss of energy and therefore a loss of amplitude. In order to analyze the contribution of each vibration peak to the overall signal and amplitude and their impact on defect size, the sum of the peak frequencies and the integrated amplitude of these two peaks are presented in Table 7. Specifically, the total values of Peak 1 and Peak 2 show that the no-defect samples have a higher integrated amplitude of 583.826 $\times$ 10^3 Hz.mV and a lower combined peak frequency of 1466.16 Hz. As there are no internal losses, acoustic waves propagate without being reflected, scattered, or absorbed. As a result, the structure retains all its energy, resulting in a low peak frequency and maximum integral amplitude. Samples with 7 and 10 mm defects, on the other hand, have a lower integrated amplitude values and higher sum of peak frequencies values. This indicates that concentrating vibrations on a smaller zone enhances the modal frequency detected. Moreover, for a smaller integrated amplitude, concentration in a reduced area minimizes the displacement of the normal surface and the energy transmitted to the air, resulting in a lower acoustic amplitude.

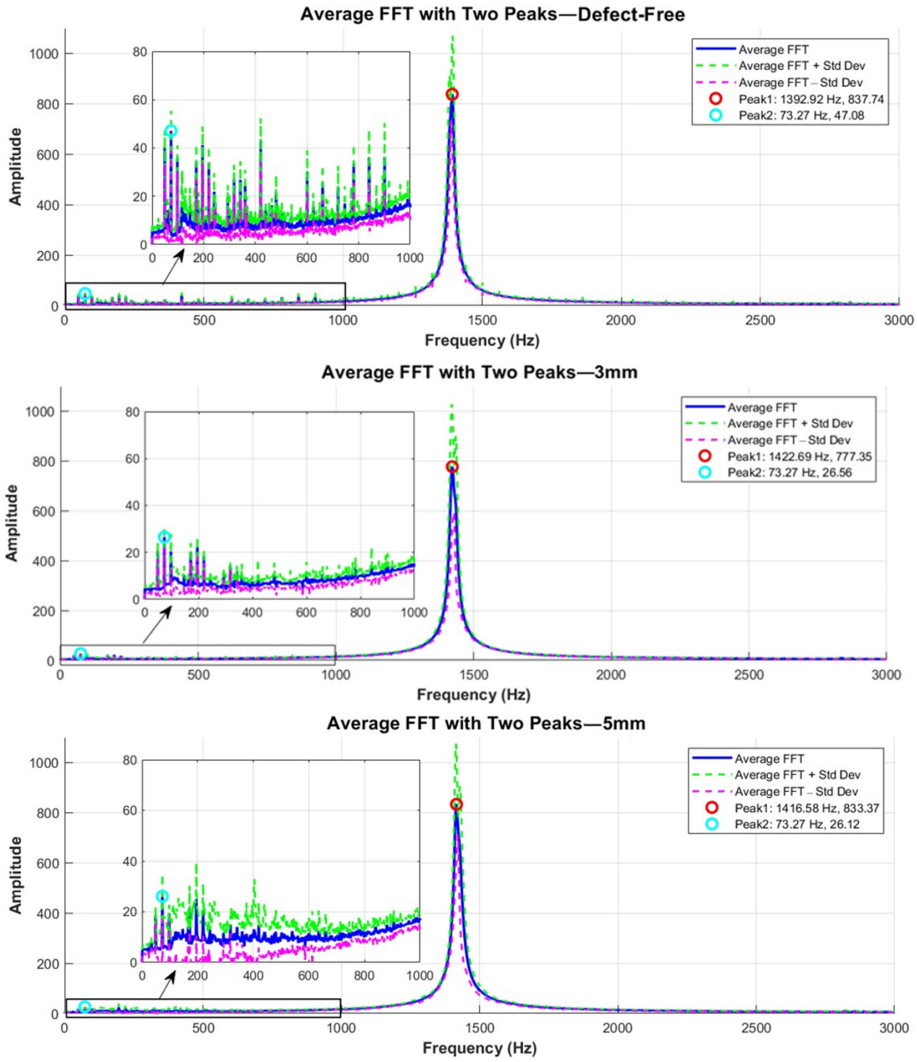

Figure 12. *Cont.*

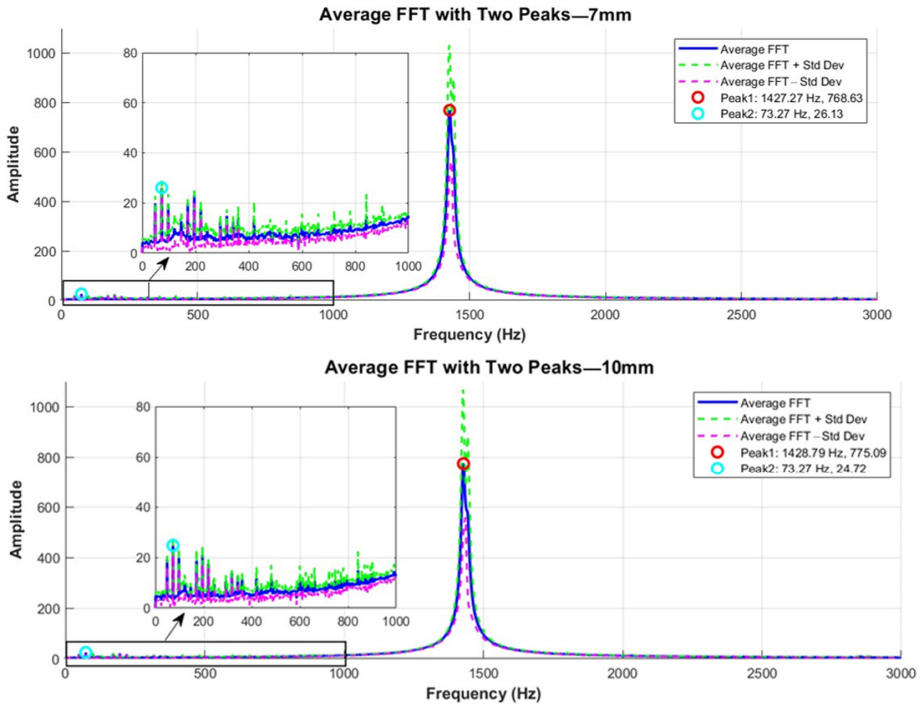

Figure 12. Comparison of the MATLAB-calculated average FFT spectra of three samples with various internal defects.

Table 7. Sum of peak frequencies and integrated amplitude for different defect sizes.

Defect Size	Acoustic	
	Sum of Peak Frequencies (Hz)	Integrated Amplitude (Hz.mV)
No defect	1466.16	583.826×10^3
3 mm	1495.96	542.406×10^3
5 mm	1489.85	577.280×10^3
7 mm	1500.54	538.052×10^3
10 mm	1502.06	542.079×10^3

- Vibration detector

Average values of peak frequency and damping, as well as their standard deviations, in relation to defect size, are presented in Table 8. A 3 mm defect shows an enhanced peak frequency. This suggests that local hardening results in little radiation disturbance and therefore elevated peak frequencies. Samples free of defects also show a higher damping value and lower frequency peak. This is due to internal manufacturing stress, which slows down vibration compared to defective parts.

Table 8. Averaging frequency peak and damping using vibration detector as a function of defect size.

Test Type	Vibration Test									
Defect Size	Defect-Free		3 mm		5 mm		7 mm		10 mm	
	Average	Standard Deviation	Average	Standard Deviation	Average	Standard Deviation	Average	Standard Deviation	Average	Standard Deviation
Frequency peak (Hz)	1392.806	4.032	1436.656	6.405	1432.317	7.128	1432.306	5.631	1434.467	7.337
Damping	56.573	14.971	27.330	2.983	25.385	0.615	26.167	0.562	26.135	1.748

Figure 13 shows the peak frequency as a function of the defect size in the flexion test. The results display that the vibration sensor detects defects as small as 3 mm, where a frequency of 1436.66 Hz is recorded, indicating that there is a high detection threshold for identifying internal defects associated with local hardening. This suggests that neural line defects with local hardening at the edge increase bending stiffness and also contribute to increased peak frequency due to the local reinforcement that can be created when defect edges touch. Additionally, a minor shift in frequency is seen at 5, 7, and 10 mm defects. Since the thickness of defects remains constant during bending, increasing their size has a limited impact on the vibration peak frequency. In addition, the error bars overlap between 3 and 10 mm flaws, indicating that increasing the defect size beyond 3 mm has little effect on peak frequency.

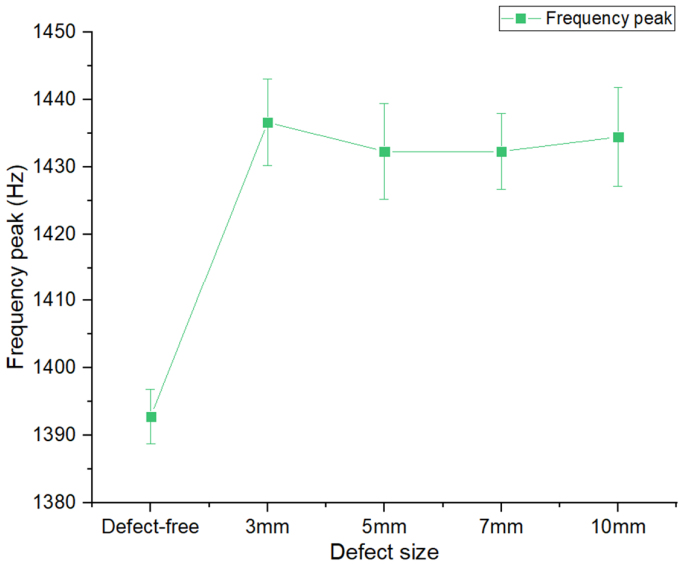

Figure 13. Frequency peak as function of defect size.

The damping effect on the defect size with the vibration sensor is shown in Figure 14. As demonstrated, as the defect size rises from no defect to 5 mm of defect, the damping decreases. However, a small rise is seen from 5 to 7 mm. As observed, when the defect size increases from a fully dense state (no defect) to 5 mm, the damping decreases. This decline suggests that the position of the defect on the neutral bending line and minimal defect volume change diminish damping. For defect sizes like 7 and 10 mm, the presence of delamination (Figure 7d,e) generates minor internal friction, resulting in minimal energy loss, which moderately improves damping. Similarly to peak frequency, damping varies very little beyond 3 mm of defect. Damping values are therefore directly influenced by the observed frequency changes (see Figure 13), with the damping having been calculated using Equation (1). Hence, the vibration detector is highly sensitive to structural changes, such as delamination and defects positioned at the neutral line, due to a distinct variation in modal properties.

Figure 15 presents the mean FFT curves for each defect size. As presented in Figure 15, Peak 2 for the vibration detector is also observed at a consistent frequency of 73.27 Hz across the no-defect sample and all defect sizes. As stated above, Peak 2 can be attributed to the defect location on the neutral bending line, which justifies the lack of frequency variation. However, a similar decreasing trend in the amplitude of Peak 2 is observed as the defect size grows from no defect to 7 mm followed by a slight increase to 56.02 mV for a 10 mm defect. In this case, the central fault causes a dispersion of vibratory energy, which reduces the energy transmitted to the vibration sensor, resulting in lower amplitude. A slight rise in amplitude from 7 to 10 mm may be linked to delamination, which can lead to

more efficient vibration of the part, resulting in a slight gain in amplitude. In addition, the amplitude values obtained with the vibration sensor are greater than those obtained with the acoustic sensor. This can be elucidated by the fact that the vibration sensor measures displacement directly and this detector is more sensitive to small movements than an acoustic sensor. Since the vibration sensor follows the local movement of the structure, there is a richer presence of numbers of vibrational harmonics in 0 to 1000 HZ than the acoustic sensor, which filters more. The sum of peak frequencies and integrated amplitude of these two peaks offers insights into the influence of the defect size on the FFT response, as summarized in Table 9. In addition, for the samples free of defects, the values for Peak 1 and Peak 2 readings show a lower combined peak frequency of 1463.9 Hz and a greater integrated amplitude of 739.954 $\times$ 10^3 Hz.mV. This is due to a coherent vibration structure with no modal loss. In addition, the 3 mm defect samples display an enhanced sum peak frequency of 1507.47 Hz. For a 3 mm defect, the high sum peak frequencies are linked to localized reinforcement, which enhances the part's rigidity. Nevertheless, samples with a 10 mm defect exhibit the lesser integrated amplitude of 589.041 $\times$ 10^3 Hz.mV. In this regard, delamination creates local decoupling, introducing a loss of vibratory energy in the damaged zone and leading to low amplitude.

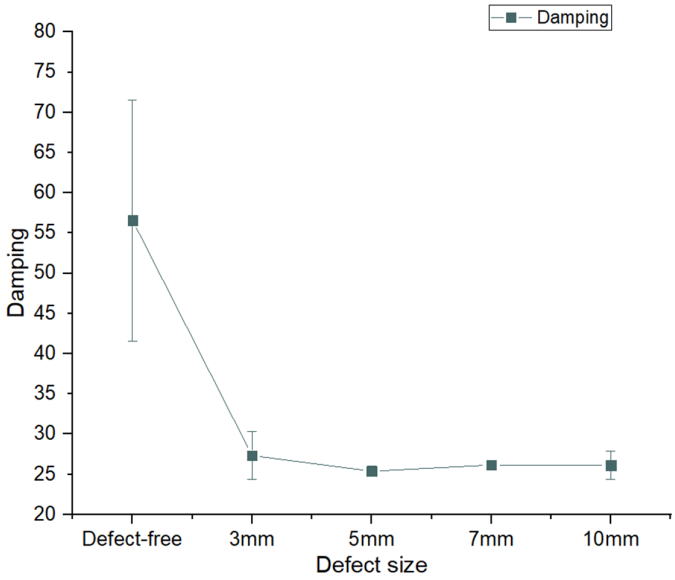

Figure 14. Correlation between damping and defect size.

Table 9. Relationship between defect size and sum of peak frequencies and integrated amplitude.

Defect Size	Vibration	
	Sum of Peak Frequencies (Hz)	**Integrated Amplitude (Hz.mV)**
No defect	1463.9	739.954 $\times$ 10^3
3 mm	1507.41	603.743 $\times$ 10^3
5 mm	1501.3	590.133 $\times$ 10^3
7 mm	1502.83	614.860 $\times$ 10^3
10 mm	1503.27	589.041 $\times$ 10^3

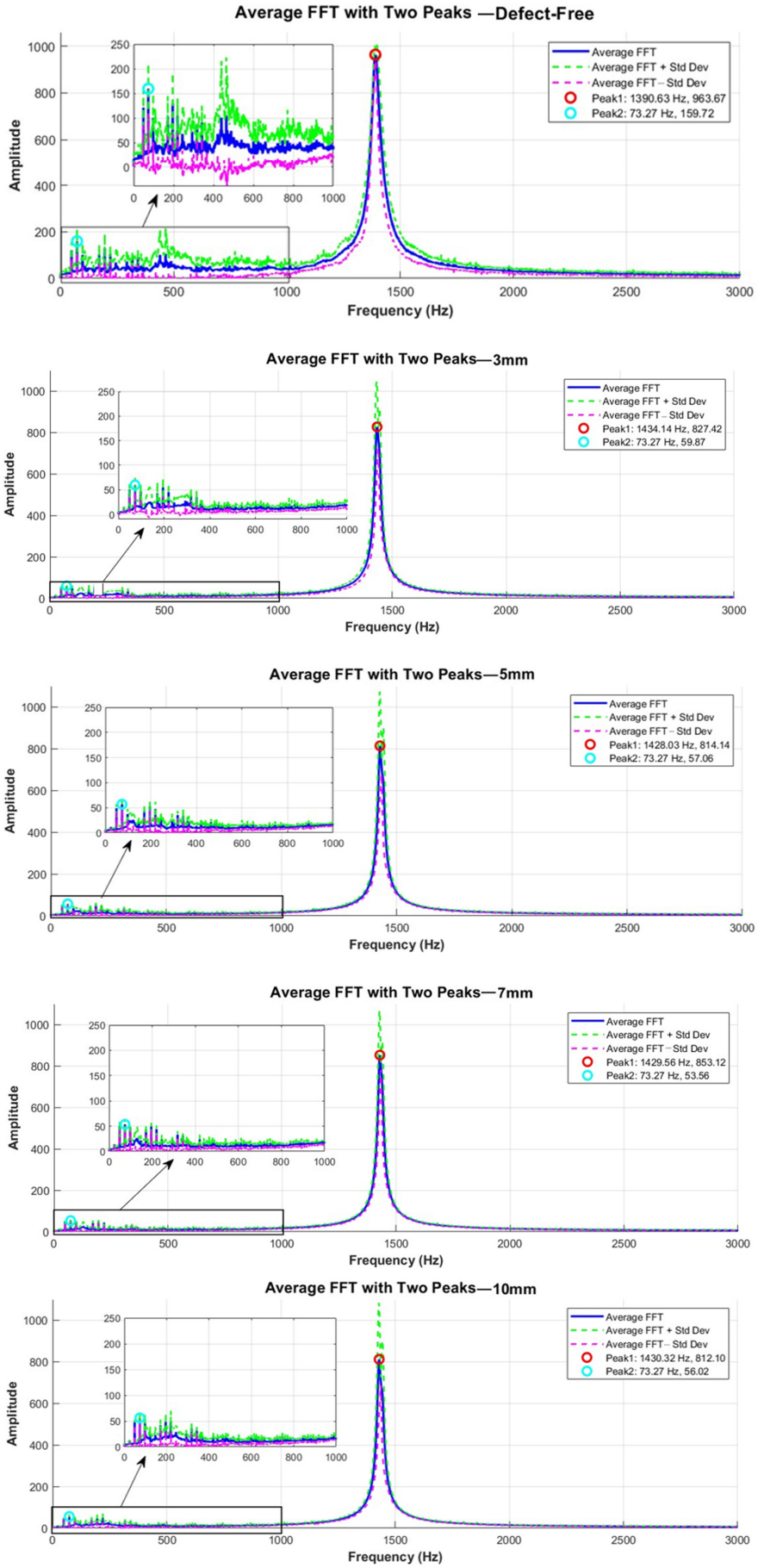

Figure 15. Analysis of three samples' average Fourier transform spectra with different types of internal defects using MATLAB.

4. Conclusions

This research aims to examine the acoustic and vibrational characteristics of 3D-printed components in relation to the size of internal flaws localized at the neutral line. The objective is to determine the contribution of defect size, position, and modal responses, including peak frequency, damping, and amplitude. Therefore, in flexion mode, this study evaluates parts with defects ranging from 3 mm to 10 mm. The results indicate that these defects have a modest effect on the modal parameters. For both detectors, increasing defects above 3 mm has little effect on peak frequency. Furthermore, in the absence of faults, both sensors exhibit a weak frequency peak and an elevated amplitude. According to the acoustic detector, small flaws of 3 to 5 mm improve damping more than parts with no defects. Despite delamination, this sensor showed reduced damping, amplitude, and elevated peak frequencies with 7 and 10 mm defects. At the 7 mm and 10 mm defects, on the other hand, the vibration sensor clearly identifies the delamination with a minor increase in damping. In addition, the neutral line location causes damping to decrease as the defect size rises by up to 5 mm. Small flaws (3 mm) with local hardening at the edge cause elevated peak frequency. Therefore, this study highlights the importance of performing further experiments with other materials and different kinds of defects, such as fractures and porosity, to have a clearer understanding of the detectors' detection sensitivity and variance. In this context, vibration sensors have the ability to detect delamination and local hardening along the neutral axis compared to acoustic detectors. However, both sensors struggle to detect frequency changes in defects larger than 3 mm. Additionally, the sensors only examine one specific closed internal defect shape and concentrate on defects that are very small compared to the overall shape of the part. In this regard, the overall size of the samples and number of samples are two additional factors that may significantly affect the modal characteristics. Accordingly, coupled finite element modeling (FEM) would shed more light on the propagation of stress waves and the localized impacts induced by the type and location of defects. In this approach, future study may employ FEM analysis to validate and support experimental results.

Author Contributions: Conceptualization, A.D. and F.-E.J.; methodology, A.D., F.-E.J. and I.O.; validation, A.D.; formal analysis, A.D. and F.-E.J.; investigation, F.-E.J.; data curation, F.-E.J.; writing—original draft preparation, F.-E.J.; writing—review and editing, A.D., R.E.A. and F.D.; supervision, A.D.; project administration, A.D.; funding acquisition, A.D. All authors have read and agreed to the published version of the manuscript.

Funding: This research received no external funding.

Institutional Review Board Statement: Not applicable.

Informed Consent Statement: Not applicable.

Data Availability Statement: The raw data supporting the conclusions of this article will be made available by the authors on request.

Acknowledgments: The authors would like to thank the Wallonie Aerotraining Network for supporting this work.

Conflicts of Interest: The authors declare no conflicts of interest.

References

1. Dimitrellou, S.; Iakovidis, I.; Psarianos, D.-R. Mechanical Characterization of Polylactic Acid, Polycarbonate, and Carbon Fiber-Reinforced Polyamide Specimens Fabricated by Fused Deposition Modeling. *J. Mater. Eng. Perform.* **2024**, *33*, 3613–3626. [CrossRef]
2. Knoop, F. Mechanical and Thermal Properties of FDM Parts Manufactured with Polyamide 12. In Proceedings of the 26th Annual International Solid Freeform Fabrication Symposium—An Additive Manufacturing Conference, Austin, TX, USA, 10–12 August 2015; Volume 10, pp. 935–948.

3. Bhong, M.; Khan, T.K.H.; Devade, K.; Vijay Krishna, B.; Sura, S.; Eftikhaar, H.K.; Pal Thethi, H.; Gupta, N. Review of Composite Materials and Applications. *Mater. Today Proc.* **2023**, *129*, S2214785323049313. [CrossRef]
4. Nicolais, L.; Gloria, A.; Ambrosio, L. The Mechanics of Biocomposites. In *Biomedical Composites*; Elsevier: Amsterdam, The Netherlands, 2010; pp. 411–440. ISBN 978-1-84569-436-4.
5. Ashebir, D.A.; Hendlmeier, A.; Dunn, M.; Arablouei, R.; Lomov, S.V.; Di Pietro, A.; Nikzad, M. Detecting Multi-Scale Defects in Material Extrusion Additive Manufacturing of Fiber-Reinforced Thermoplastic Composites: A Review of Challenges and Advanced Non-Destructive Testing Techniques. *Polymers* **2024**, *16*, 2986. [CrossRef]
6. Erokhin, K.; Naumov, S.; Ananikov, V. Defects in 3D Printing and Strategies to Enhance Quality of FFF Additive Manufacturing. A Review. *Mater. Sci.* **2023**, *92*, 123–145. [CrossRef]
7. Baechle-Clayton, M.; Loos, E.; Taheri, M.; Taheri, H. Failures and Flaws in Fused Deposition Modeling (FDM) Additively Manufactured Polymers and Composites. *J. Compos. Sci.* **2022**, *6*, 202. [CrossRef]
8. Sadaf, A.I.; Ahmed, H.; Khan, M.A.I.; Sezer, H. Development of Real-Time Defect Detection Techniques Using Infrared Thermography in the Fused Filament Fabrication Process. In Proceedings of the ASME 2023 International Mechanical Engineering Congress and Exposition: Volume 3: Advanced Manufacturing, New Orleans, LA, USA, 29 October–2 November 2023; p. V003T03A017.
9. Gallardo, D.; Díaz, L.-C.; Jiménez, R.; Torralba, M.; Albajez, J.A.; Fabra, J.A.Y. X-Ray Computed Tomography Performance in Metrological Evaluation and Characterisation of Polymeric Additive Manufactured Surfaces. *Addit. Manuf.* **2023**, *75*, 103754. [CrossRef]
10. Saddoud, R.; Sergeeva-Chollet, N.; Darmon, M. Eddy Current Sensors Optimization for Defect Detection in Parts Fabricated by Laser Powder Bed Fusion. *Sensors* **2023**, *23*, 4336. [CrossRef] [PubMed]
11. Quader, R.; Klinstein, L.; Grewell, D.; Narayanan, L.K. Evaluation of the Influence of Ultrasonic Vibration on Physical, Tensile, and Morphological Properties of Fused Deposition Modeled Specimens. *Int. J. Adv. Manuf. Technol.* **2024**, *132*, 1095–1109. [CrossRef]
12. Gomes, P.C.; Piñeiro, O.G.; Alves, A.C.; Carneiro, O.S. On the Reuse of SLS Polyamide 12 Powder. *Materials* **2022**, *15*, 5486. [CrossRef]
13. Georgeson, G.E.; Lea, S.; Hansen, J. *Electronic Tap Hammer for Composite Damage Assessment*; Rempt, R.D., Broz, A.L., Eds.; Proceedings of SPIE, Vol. 2945, Nondestructive Evaluation of Aging Aircraft, Airports, and Aerospace Hardware; SPIE: Scottsdale, AZ, USA, 1996; pp. 328–338.
14. Heritage, K.; Frisby, C.; Wolfenden, A. Impulse Excitation Technique for Dynamic Flexural Measurements at Moderate Temperature. *Rev. Sci. Instrum.* **1988**, *59*, 973–974. [CrossRef]
15. Popov, I.I.; Shitikova, M.V. Impulse Excitation Technique and Its Application for Identification of Material Damping: An Overview. *IOP Conf. Ser. Mater. Sci. Eng.* **2020**, *962*, 022025. [CrossRef]
16. Nasimi, R.; Atcitty, S.; Thompson, D.; Murillo, J.; Ball, M.; Stormont, J.; Moreu, F. Use of Remote Structural Tap Testing Devices Deployed via Ground Vehicle for Health Monitoring of Transportation Infrastructure. *Sensors* **2022**, *22*, 1458. [CrossRef]
17. Shekhar, S.; Ozdoganlar, O.B. Reproducible Modal Testing Using a Flexure-Based Impact Excitation System. In *Topics in Modal Analysis & Testing*; Mains, M.L., Dilworth, B.J., Eds.; Conference Proceedings of the Society for Experimental Mechanics Series; Springer International Publishing: Cham, Switzerland, 2020; Volume 8, pp. 349–352. ISBN 978-3-030-12683-4.
18. Coffey, E. Acoustic Resonance Testing. In Proceedings of the 2012 IEEE Future of Instrumentation International Workshop (FIIW) Proceedings, Gatlinburg, TN, USA, 8–9 October 2012; pp. 1–2.
19. Iliopoulos, S.; Iliopoulos, A.; Pyl, L.; Sol, H.; Aggelis, D.G. *A Qualitative and Quantitative Investigation of the Uncracked and Cracked Condition of Concrete Beams Using Impulse Excitation, Acoustic Emission, and Ultrasonic Pulse Velocity Techniques*; Ecke, W., Peters, K.J., Meyendorf, N.G., Matikas, T.E., Eds.; Proceedings of SPIE Volume 9062, "Smart Sensor Phenomena, Technology, Networks, and Systems Integration 2014"; SPIE: San Diego, CA, USA, 2014; p. 90620Q.
20. Cascante, G.; Santamarina, C.; Yassir, N. Flexural Excitation in a Standard Torsional-Resonant Column Device. *Can. Geotech. J.* **1998**, *35*, 3. [CrossRef]
21. Yew, C.H.; Chen, C.S. Study of Linear Wave Motions Using FFT and Its Potential Application to Non-Destructive Testing. *Int. J. Eng. Sci.* **1980**, *18*, 1027–1036. [CrossRef]
22. Jalili, M.M.; Mousavi, S.Y.; Pirayeshfar, A.S. Flexural Free Vibration as a Non-Destructive Test for Evaluation of Viscoelastic Properties of Polymeric Composites in Bending Direction. *Iran. Polym. J.* **2014**, *23*, 327–333. [CrossRef]
23. Jalili, M.M.; Pirayeshfar, A.S.; Mousavi, S.Y. A Comparative Study on Viscoelastic Properties of Polymeric Composites Measured by a Longitudinal Free Vibration Non-Destructive Test and Dynamic Mechanical Thermal Analysis. *Iran. Polym. J.* **2012**, *21*, 651–659. [CrossRef]
24. Brown, D.L.; Allemang, R.J.; Halvorsen, W.G. Impulse Technique for Structural Frequency Response Testing. *J. Acoust. Soc. Am.* **1978**, *63*, S81. [CrossRef]
25. Wu, H.; Siegel, M. Correlation of Accelerometer and Microphone Data in the "Coin Tap Test". *IEEE Trans. Instrum. Meas.* **2000**, *49*, 493–497. [CrossRef]

26. Raza, A.; Rimašauskienė, R.; Jūrėnas, V.; Mahato, S. Experimental Investigation of Vibration Amplitude Control in Additive Manufactured PLA and PLA Composite Structures with MFC Actuator. *Eng. Struct.* **2023**, *294*, 116802. [CrossRef]
27. Benabderazag, K.; Belouadah, Z.; Guebailia, M.; Toubal, L. Characterization of Thermomechanical Properties and Damage Mechanisms Using Acoustic Emission of Lygeum Spartum PLA 3D-Printed Biocomposite with Fused Deposition Modelling. *Compos. Part A Appl. Sci. Manuf.* **2024**, *186*, 108426. [CrossRef]
28. Bhudolia, S.K.; Gohel, G.; Leong, K.F.; Joshi, S.C. Damping, Impact and Flexural Performance of Novel Carbon/Elium® Thermoplastic Tubular Composites. *Compos. Part B Eng.* **2020**, *203*, 108480. [CrossRef]
29. Vigneshwaran, K.; Venkateshwaran, N.; Shanthi, R.; Kannan, G.; Kumar, B.R.; Shanmugam, V.; Das, O. The Acoustic Properties of FDM Printed Wood/PLA-Based Composites. *Compos. Part C Open Access* **2024**, *15*, 100532. [CrossRef]
30. Liu, F.; Gao, Q.; Guo, H.; Lang, C.; Jiang, J.; Qiu, Y. A Test Method for Acoustic Emission Properties of Natural Cellulose Fiber-Reinforced Composites. *Appl. Sci.* **2021**, *11*, 12067. [CrossRef]
31. Heinrich, M.; Valeske, B.; Rabe, U. Efficient Detection of Defective Parts with Acoustic Resonance Testing Using Synthetic Training Data. *Appl. Sci.* **2022**, *12*, 7648. [CrossRef]
32. Beheshtizadeh, N.; Mostafapour, A. Characterization of Carbon Fiber/Epoxy Composite Damage by Acoustic Emission Using FFT and Wavelet Analysis. *Adv. Eng. Forum* **2016**, *17*, 77–88. [CrossRef]
33. *ISO 1183-1: 2025*; Plastics—Methods for Determining the Density of Non-Cellular Plastics. International Organization for Standardization: Geneva, Switzerland, 2025.
34. *ASTM E1876-22*; Standard Test Method for Dynamic Youngs Modulus, Shear Modulus, and Poissons Ratio by Impulse Excitation of Vibration. E28 Committee ASTM International: West Conshohocken, PA, USA, 2022. [CrossRef]